Mirror symmetry and cluster structures of resonant states in ^{9}Be and ^{9}B

Myagmarjav Odsuren,[1,*] Yuma Kikuchi,[2,†] Takayuki Myo,[3,4,‡] and Kiyoshi Katō[5,§]
[1]School of Engineering and Technology, National University of Mongolia, Ulaanbaatar 210646, Mongolia
[2]Tokuyama College, National Institute of Technology, Yamaguchi 745-8585, Japan
[3]General Education, Faculty of Engineering, Osaka Institute of Technology, Osaka 535-8585, Japan
[4]Research Center for Nuclear Physics (RCNP), Osaka University, Ibaraki 567-0047, Japan
[5]Nuclear Reaction Data Centre, Faculty of Science, Hokkaido University, Sapporo 060-0810, Japan

(Received 15 December 2025; accepted 26 January 2026; published 17 February 2026)

We apply the complex-scaling method (CSM) to the $\alpha + \alpha + N$ three-body model to study the nuclear structure of ^{9}Be and ^{9}B nuclei, focusing mainly on mirror symmetry in the resonant states. In our previous paper [Phys. Rev. C **110**, 064316 (2024)], we reported the energy-level structure below about 15 MeV excitation energy in ^{9}Be and ^{9}B nuclei and discussed the significant effect of the Coulomb force. In this paper, we investigate the wave functions of these states, i.e., the matter- and charge-distribution radii, and the cluster-channel amplitudes. The results show a clear mirror-symmetry breaking between ^{9}Be and ^{9}B nuclei, which is mainly due to the Coulomb interaction.

DOI: 10.1103/2kn8-vd5t

I. INTRODUCTION

The low-lying states of the mirror nuclei ^{9}Be and ^{9}B have been a subject of continuous interest, both theoretically [1–9] and experimentally [10–15], due to their curious nuclear structure. The valence nucleon around two α clusters is believed to occupy a p orbital in the ground state and possibly an s orbital in excited states.

The first unbound excited $1/2^+$ state in these mirror nuclei has been extensively investigated using various theoretical approaches [16,17] and experimental methods [18,19]. We have successfully described the structure of the $1/2^+$ state using an $\alpha + \alpha + N$ three-body model and the complex-scaling method (CSM) [20–28]. We found that the excited $1/2^+$ state in ^{9}Be has a virtual-state character, whereas in ^{9}B, the Coulomb potential leads to a mirror-symmetry breaking, resulting in two distinct $1/2^+$ resonant states [20–22].

This intriguing phenomenon motivates a wide investigation into the mirror symmetry of other low-lying states. The primary difference between the mirror nuclei ^{9}Be and ^{9}B is the Coulomb interaction between the α clusters and the valence nucleon, which alters the spatial distributions and causes systematic energy shifts of the nuclei.

*Contact author: odsuren@num.edu.mn
†Contact author: kikuchi@tokuyama.ac.jp
‡Contact author: takayuki.myo@oit.ac.jp
§Contact author: kato@nucl.sci.hokudai.ac.jp

This work extends our previous calculations [1] to investigate the mirror resonances of both odd-parity states ($J^\pi = 1/2^-$ to $9/2^-$) and even-parity states ($J^\pi = 1/2^+$ to $9/2^+$) below the 15 MeV excitation energy. Those calculated states are classified into the C type and E type due to the size of the Coulomb energy shifts and into several band states as follows:

(1) C type: $K^\pi = 3/2^-_{g.s.}$-, $1/2^-_1$- and $1/2^+$-band states at low energies and with a large Coulomb-energy shift,
(2) E type: $K^\pi = 1/2^-_{2,3,4}$- and $3/2^+$-band states in high energies and with a small Coulomb-energy shift.

The three low-lying bands belonging to the C type have some experimental data and have been reproduced by other calculations. However, high-lying E-type band states are new resonant states obtained in our calculation. In addition to the low-lying C-type band states, which have been studied well so far, we are interested in obtaining information and understanding of properties of the new E-type band states.

These E-type band resonant states, with broad decay widths, provide a unique opportunity to understand the multichannel decay mechanisms and distribution of cluster structures. To see the structure of such resonant states, we calculate the expectation values of the matter and charge radii and the channel amplitudes in the CSM [27]. The comparative analyses of the matter and channel radii for mirror pairs are expected to offer insights into the subtle effects of the Coulomb force on those resonant states. Furthermore, investigation of channel amplitudes in addition to matter and charge radii is useful in revealing a systematic energy shift between those band states of ^{9}Be and ^{9}B, validating the effects of the Coulomb force.

These results reveal a significant mirror-symmetry breaking in the spatial properties of these nuclei. Although many states of ^{9}Be have matter radii larger than the charge radii, similar to the neutron-rich nuclei observed, the mirror nucleus ^{9}B exhibits the opposite relationship, with a consistently larger charge radius. This is a direct consequence of Coulomb repulsion moving the valence proton away from the di-α core, indicating a significant spatially extended structure of the proton.

This paper is organized as follows: Sec. II describes the theoretical framework of our $\alpha+\alpha+N$ three-body model and the complex scaling method. In Sec. III, we present and discuss the results of our calculations, including the systematic energy shifts, the comparison of matter and charge radii, and the analysis of channel amplitude. Section IV presents some discussion of the results obtained, and a summary and conclusions are given in Sec. V.

II. THEORETICAL FRAMEWORK

A. $\alpha+\alpha+N$ model and complex scaling method

The $\alpha+\alpha+N$ three-body model is used to simultaneously solve the bound and resonant states in ^{9}Be and ^{9}B nuclei. The antisymmetrization effect is also described using the orthogonal-condition model (OCM) [29]. For details, see the previous paper [21]. In this paper, to study the properties of the resonant states of $A=9$ mirror nuclei, we use the theoretical framework of the analysis of wave functions in the complex-scaling method (CSM) [23–26], in which the relative coordinates $(\mathbf{r},\mathbf{R})$ in the Hamiltonian are transformed into $(\mathbf{r}e^{i\theta},\mathbf{R}e^{i\theta})$ with a real scaling angle θ by the transformation operator $U(\theta)$.

Basically, it is the same as the treatment of bound states, but the big difference is that the states in bra space are not Hermite conjugates of the states in ket space but are biorthogonal conjugates [27]. The bound and resonant states are commonly obtained by solving the complex-scaled Schrödingier equation expressed as

$$\hat{H}^\theta\Psi^k_{J^\pi}(\theta)=E^\theta_k\Psi^k_{J^\pi}(\theta). \tag{1}$$

The complex-scaled Hamiltonian $\hat{H}^\theta$ and the wave function $\Psi^k_{J^\pi}(\theta)$ are defined as $U(\theta)HU(\theta)^{-1}$ and $U(\theta)\Psi^k_{J^\pi}$, respectively [26], where k is a state index.

Due to the complex scaling, a resonance wave function is regularized and can be described by square-integrable functions. As square-integrable basis functions, we employ Gaussian functions [30], and then the three-body wave function is expressed by a sum of wave functions in different Jacobi coordinate systems as

$$\begin{aligned}\Psi^{J^\pi}_k(\theta)&=\sum_{\nu_Y}C^k_{\nu_Y}(\theta)\big|\big[\big[\phi_{l_1}\big(\mathrm{r}_1;a^i_1\big)\otimes\phi_{L_1}\big(\mathrm{R}_1;a^i_2\big)\big]_{\Lambda_1}\otimes\chi^\sigma_{1/2}\big]_J\big\rangle\\&+\sum_{\nu_T}C^k_{\nu_T}(\theta)\big|\big[\big[\phi_{l_2}\big(\mathrm{r}_2;a^j_1\big)\otimes\phi_{L_2}\big(\mathrm{R}_2;a^j_2\big)\big]_{\Lambda_2}\otimes\chi^\sigma_{1/2}\big]_J\big\rangle,\end{aligned} \tag{2}$$

where $C^k_{\nu_Y}(\theta)$ and $C^k_{\nu_T}(\theta)$ are expansion coefficients and $\chi_{\frac{1}{2}}$ is the spin wave function of the valence nucleon. The relative coordinates $\{\mathbf{r_c},\mathbf{R_c}\}$ $(c=1,2)$ of the three-body model $\alpha+\alpha+N$ are given in two types of Jacobi coordinate systems (type Y and type T) indexed by $c(=1,2)$, respectively, as shown in Fig. 1. The operator $\mathcal{S}$ is a symmetrizer between two α particles. The function $\phi_l(r;a)$ is a Gaussian basis function with the range parameter a, which is given by

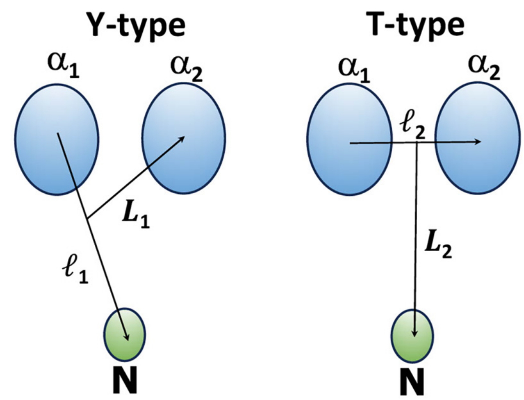

FIG. 1. Schematic illustration of the Y- and T-type Jacobi coordinate sets of the $\alpha+\alpha+N$ system.

$$\phi_l(r;a)=r^l\exp\left(-\tfrac{1}{2}ar^2\right)Y_l(\hat{r}). \tag{3}$$

The indices ν_Y and ν_T are sets of $\{l_1,L_1,\Lambda_1,i\}$ and $\{l_2,L_2,\Lambda_2,j\}$, respectively.

The expectation values of these radii are calculated as

$$\langle\hat{R}^2\rangle=\big\langle\tilde{\Psi}^\nu_{J^\pi}\big|\hat{R}^2\big|\Psi^\nu_{J^\pi}\big\rangle, \tag{4}$$

where $\tilde{\Psi}^\nu_{J^\pi}$ is the biorthogonal conjugate state of $\Psi^\nu_{J^\pi}$. The root-mean-square radius is obtained as $R=\sqrt{\langle\hat{R}^2\rangle}$ for matter and charge parts in this paper [31]. The value of the root-mean-square radius is a real number for the bound state but a complex number for the resonant state, and the physical meanings have been discussed in our recent paper [27]. Generally, resonant states with sharp widths show small values of the imaginary part. In this study, we investigate the properties of the resonant states by taking the real part of the calculated radii.

B. Channel amplitudes

We calculate channel amplitudes to see the structures of the bound and resonant states in ^{9}Be and ^{9}B. The channels of the $\alpha+\alpha+N$ model are expressed by angular-momentum couplings of relative motions of clusters and a spin of a nucleon in the two Jacobi coordinates, as shown in Fig. 1. The channel wave functions are defined as

$$h^{YJ}_{c_Y}=\big[\big[Y_{l_1}(\hat{r}_1)\otimes\chi^\sigma_{1/2}\big]_{I^\pi_1}\otimes Y_{L_1}(\hat{R}_1)\big]_J \tag{5}$$

for the Y-type [(α_1-N)-α_2] coordinate system and

$$h^{TJ}_{c_T}=\big[Y_{l_2}(\hat{r}_2)\otimes\big[Y_{L_2}(\hat{R}_2)\otimes\chi^\sigma_{1/2}\big]_{I^\pi_2}\big]_J \tag{6}$$

for the T-type [(α_1-α_2)-N] one, where $c_Y=\{l_1,L_1,I_1\}$ and $c_T=\{l_2,L_2,I_2\}$.

To calculate channel amplitudes, we define projection operators $\hat{P}_{c_Y}$ and $\hat{P}_{c_T}$ for channels c_Y and c_T, respectively, as

TABLE I. Calculated resonance energies ($E^{\rm res}$), decay widths ($\Gamma^{\rm res}$), and complex-valued matter (R_m) and charge (R_{ch}) radii for the odd spin-parity states of the mirror nuclei ^{9}Be and ^{9}B. Energy, matter, and charge radii are given in comparison with experiments for the ground state of ^{9}Be.

	CAL. ^{9}Be		Matter radii ^{9}Be		Charge radii ^{9}Be		Charge radii ^{9}B		Matter radii ^{9}B		CAL. ^{9}B	
	$E^{\rm res}_{J^\pi}$ [MeV]	$\Gamma^{\rm res}_{J^\pi}$ [MeV]	Re(R_m) [fm]	Im(R_m) [fm]	Re(R_{ch}) [fm]	Im(R_{ch}) [fm]	Re(R_{ch}) [fm]	Im(R_{ch}) [fm]	Re(R_m) [fm]	Im(R_m) [fm]	$E^{\rm res}_{J^\pi}$ [MeV]	$\Gamma^{\rm res}_{J^\pi}$ [MeV]
$3/2^-_{g.s.}$	–2.15 (–1.57[a])	–	2.41 (2.38[b])	–	2.50 (2.52[c])	–	2.77	–	2.51	–	– 0.22	–
$3/2^-_2$	2.73	0.84	3.10	1.17	2.79	0.84	2.95	1.02	2.67	0.90	4.10	1.50
$3/2^-_3$	5.80	3.70	5.74	1.56	3.13	0.71	7.20	2.16	5.69	1.70	6.23	3.94
$3/2^-_4$	7.43	5.90	3.98	1.28	2.72	0.64	4.91	1.60	3.99	1.28	7.95	6.20
$3/2^-_5$	7.40	8.00	5.77	2.53	3.26	1.39	7.27	3.27	5.79	2.62	7.80	8.30
$5/2^-_1$	0.19	4.0×10^{-3}	2.14	0.04	2.31	0.03	2.88	0.05	2.63	0.04	2.05	8.0×10^{-3}
$5/2^-_2$	6.06	1.74	2.24	0.15	2.38	0.13	2.49	0.16	2.26	0.18	8.04	2.18
$5/2^-_3$	8.60	9.80	3.64	3.83	2.01	2.35	3.67	4.96	2.81	4.15	9.00	10.20
$5/2^-_4$	16.45	8.46	5.17	1.65	2.80	0.67	6.58	2.14	5.18	1.68	16.80	8.66
$1/2^-_1$	0.98	0.42	6.36	6.62	3.40	2.07	7.32	−0.50	5.86	−0.37	2.61	0.96
$1/2^-_2$	5.70	3.60	4.15	1.70	2.24	1.07	5.23	1.96	4.08	1.61	6.15	3.80
$1/2^-_3$	7.15	7.30	5.58	2.09	2.92	0.63	7.12	2.87	5.57	2.20	7.50	7.60
$1/2^-_4$	8.40	11.80	5.81	4.97	2.91	3.27	7.24	6.38	5.63	5.32	8.75	12.40
$7/2^-_1$	4.21	0.75	2.17	0.25	2.34	0.22	2.40	0.24	2.19	0.25	6.32	1.24
$7/2^-_2$	8.20	7.44	4.88	1.89	2.83	0.79	6.15	2.47	4.87	1.93	8.55	7.74
$7/2^-_3$	9.87	12.7	4.48	1.79	2.94	0.77	5.58	2.37	4.51	1.86	10.25	13.14
$7/2^-_4$	11.10	4.41	2.46	0.32	2.33	0.34	2.80	1.30	2.43	1.01	12.57	4.84
$7/2^-_5$	19.86	14.24	4.10	1.49	2.58	0.66	5.13	1.91	4.10	1.52	20.32	14.60
$9/2^-_1$	8.26	1.18	2.26	0.28	2.35	0.24	2.53	0.31	2.27	0.31	10.20	1.56
$9/2^-_2$	9.63	9.80	4.31	1.65	2.70	0.75	5.41	2.12	4.33	1.69	10.08	11.16
$9/2^-_3$	9.90	11.50	4.85	2.08	2.83	0.85	6.01	2.77	4.77	2.16	10.30	11.90
$9/2^-_4$	19.46	14.00	4.30	1.87	2.61	0.78	5.38	2.45	4.28	1.93	19.88	14.40

[a]Reference [32].
[b]Reference [33].
[c]Reference [31].

follows:

$$\hat{P}_{c_Y} = \left|h^{YJ}_{c_Y}\right\rangle\!\left\langle h^{YJ}_{c_Y}\right|, \quad \hat{P}_{c_T} = \left|h^{TJ}_{c_T}\right\rangle\!\left\langle h^{TJ}_{c_T}\right|. \tag{7}$$

Using these operators, we calculate the channel amplitude for the channel c, Z^k_c, as

$$Z^k_c = \langle \Psi_k|\hat{P}_c|\Psi_k\rangle. \tag{8}$$

We note that wave functions of the Y- and T-type channels are not orthogonal to each other, and they satisfy

$$\sum_{c_Y} Z^k_{c_Y} = 1, \quad \sum_{c_T} Z^k_{c_T} = 1. \tag{9}$$

III. RESULTS

In the previous work [1] of ^{9}Be and ^{9}B, we calculated the energy levels of odd- and even-parity states up to $J = 9/2$ and ∼10 MeV above the three-body threshold. By extending our calculations to include higher values of the quantum numbers of angular momentum (ℓ, L, Λ), we expanded the number of odd-parity states from 18 (Table I in Ref. [1]) to 22 (see Table I of this work) for each nucleus. This expansion allowed for a more precise depiction of the band structures and significantly improved our ability to analyze the resulting data.

For the even-parity states, the number of states does not increase from the previous work [1], but we can now examine their structure in more detail. As shown in Ref. [1], our calculations successfully reproduce the Coulomb-energy differences observed for the low-lying states in ^{9}Be and ^{9}B. Those states are classified into three rotational bands ($3/2^-_{g.s.}$, $1/2^-_1$, and $1/2^+$) and labeled as C-type states, which are characterized by large Coulomb-energy differences and small decay widths. In addition, states with small Coulomb-energy differences are calculated at high excitation energies as broad resonances. We termed them “E-type” states. Those results are illustrated in Fig. 2 and Fig. 3 for 44 odd-parity states and in Fig. 4 for 18 even-parity states. Figure 2 illustrates the odd-parity energy levels for the lower two bands ($K^\pi = 3/2^-_{g.s.}$ and $1/2^-_1$) of the mirror nuclei ^{9}Be (crosses) and ^{9}B

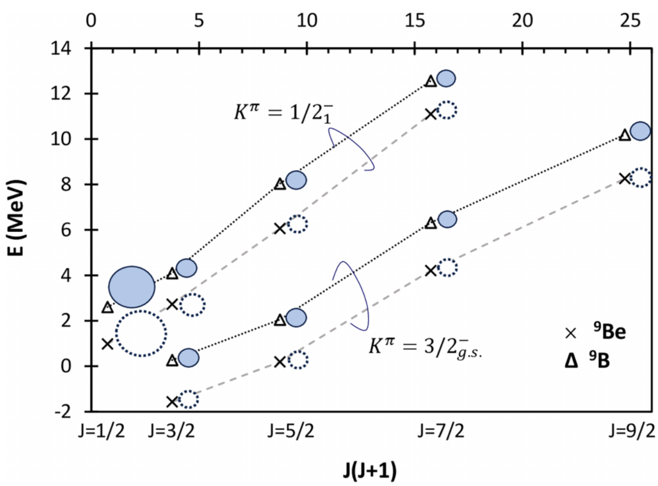

FIG. 2. The odd-parity lower-energy levels as function of $J(J+1)$ measured from the $\alpha+\alpha+N$ threshold. Open triangles and crosses display energy levels of ^{9}B and ^{9}Be, respectively. The matter radii for the ^{9}Be and ^{9}B nuclei are represented by open circles with dashed outlines and blue circles with solid outlines, respectively.

(open triangles), plotted as a function of the rotational angular momentum $J(J+1)$, and higher three bands ($K^\pi = 1/2^-_{2,3,4}$) are shown in Fig. 3. The vertical axis represents the energy measured from the $\alpha+\alpha+N$ three-body decay threshold. These results suggest a complex rotational structure of these nuclei. In particular, the E-type states shown in Fig. 3 exhibit a deviation from the typical rigid rotational behavior. The calculated matter radii for the states of ^{9}Be and ^{9}B are also displayed by open circles (dashed lines) and blue circles (solid lines), respectively.

As can be seen in Fig. 2, the calculated energy levels of ^{9}B are consistently higher than the corresponding ones of ^{9}Be. This systematic energy shifts are the direct influence of the Coulomb repulsion force of the valence proton in ^{9}B, which is absent for the valence neutron in ^{9}Be. Such Coulomb-energy differences are also observed in the "E-type" levels shown in

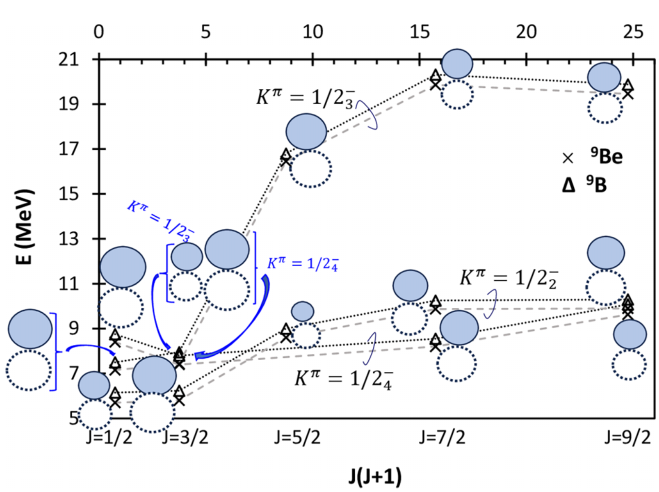

FIG. 3. The same with Fig. 2 but for odd-parity higher-energy levels.

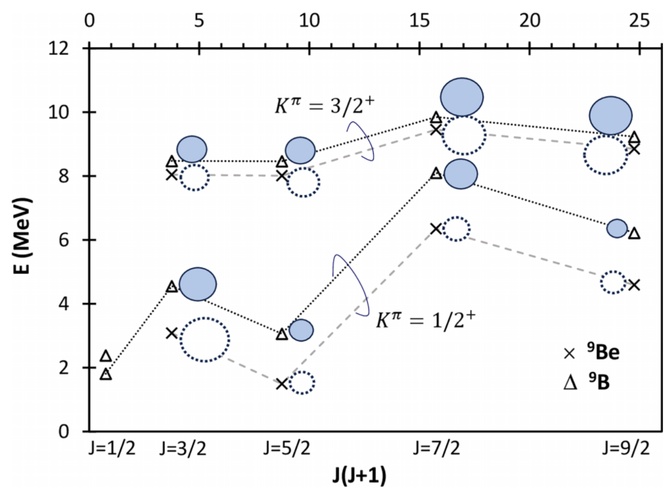

FIG. 4. The same with Fig. 2 but for even-parity energy levels.

Fig. 3 but they are much smaller than the "C-type" ones. These results indicate that "E-type" states have spatially extended configurations in comparison with more compact "C-type" configurations.

The ground-band $K^\pi = 3/2^-_{g.s.}$ states and the first excited-band $K^\pi = 1/2^-_1$ states exhibit a typical rotational pattern, confirming a spatial-deformation nature of these states. However, the significant observation is provided by the behavior of the higher-lying bands $K^\pi = 1/2^-_{2,3,4}$ shown in Fig . 3. The results show that the $K^\pi = 1/2^-_2$ and $K^\pi = 1/2^-_4$ bands intersect with the $K^\pi = 1/2^-_1$ band between the $J = 5/2^-$ and $J = 7/2^-$ states. These higher bands also overlap with the $K^\pi = 3/2^-_{g.s.}$ band at $J = 9/2^-$ in ^{9}B. Furthermore, the $K^\pi = 1/2^-_3$ and $K^\pi = 1/2^-_4$ bands cross at the low angular-momentum state $J = 3/2^-$ in both mirror nuclei. Following this first crossing, the $K^\pi = 1/2^-_4$ band sees a crossing with the $K^\pi = 1/2^-_2$ band as the angular momentum increases further.

Figure 4 shows the even-parity states of $K^\pi = 1/2^+$ and $3/2^+$ bands of the mirror nuclei ^{9}Be and ^{9}B. Here, it should be noted that the $1/2^+$ in the $K^\pi = 1/2^+$ band of ^{9}Be is not shown because it is a virtual state. The even-parity solutions consist of only these two bands. The $K^\pi = 1/2^+$ band states exhibit a large Coulomb-energy difference and are classified as the C type, while the excited $K^\pi = 3/2^+$ band consists of the E-type states. Interesting results regarding their radii are discussed in the next subsection.

A. Root-mean-square radius

The calculated expectation values of the root-mean-square radii are shown in Tables I and II for odd-party and even-parity solutions, respectively. They are obtained by applying the CSM (see Ref. [27]) for resonant states and expressed by a complex number $\mathrm{Re}(R) + i\mathrm{Im}(R)$. We consider that the real part $\mathrm{Re}(R)$ provides a physical measure of the spatial expansion of a resonant state, and the imaginary part $\mathrm{Im}(R)$ quantifies how the complex-scaled wave function diffuses into the asymptotic region. From Table I we can see that, with a few exceptions, the real part is often larger than the imaginary

TABLE II. The same with Table I but for even-parity states of ^{9}Be and ^{9}B mirror nuclei.

	CAL.		Matter radii		Charge radii				Matter radii		CAL.	
	^{9}Be		^{9}Be		^{9}Be		^{9}B		^{9}B		^{9}B	
	$E^{\mathrm{res}}_{J^\pi}$ [MeV]	$\Gamma^{\mathrm{res}}_{J^\pi}$ [MeV]	Re(R_m) [fm]	Im(R_m) [fm]	Re(R_{ch}) [fm]	Im(R_{ch}) [fm]	Re(R_{ch}) [fm]	Im(R_{ch}) [fm]	Re(R_m) [fm]	Im(R_m) [fm]	$E^{\mathrm{res}}_{J^\pi}$ [MeV]	$\Gamma^{\mathrm{res}}_{J^\pi}$ [MeV]
$1/2^+_1$	–	–	–	–	–	–	23.1	13.2	17.7	10.0	1.81	1.98
$1/2^+_2$	–	–	–	–	–	–	7.26	4.52	7.18	4.74	2.38	1.81
$5/2^+_1$	1.49	0.34	3.15	1.08	3.11	0.80	3.34	0.71	3.01	0.75	3.06	0.86
$5/2^+_2$	8.01	7.88	4.01	1.86	2.86	0.58	4.58	2.51	3.69	1.91	8.46	8.28
$3/2^+_1$	3.08	1.13	6.14	4.23	3.21	1.23	6.07	–2.28	4.75	−1.65	4.55	2.50
$3/2^+_2$	8.04	7.16	3.54	0.60	3.05	–1.07	4.50	1.43	3.75	0.68	8.47	7.60
$7/2^+_1$	6.35	6.00	3.29	1.48	2.57	0.63	5.05	8.07	4.21	6.17	8.10	8.00
$7/2^+_2$	9.45	10.20	5.30	2.12	3.18	0.95	6.62	2.75	5.30	2.17	9.85	10.60
$9/2^+_1$	4.59	2.34	2.88	0.81	2.68	0.53	2.87	0.47	2.62	0.54	6.22	3.22
$9/2^+_2$	8.85	8.92	5.37	2.08	3.03	0.87	6.77	2.72	5.37	2.13	9.23	9.24

part. So in Figs. 2–4 we visualize the real part of the matter radius as a circle.

From Table I, we find that the charge radii of ^{9}B [Re(R_c)] are consistently larger than not only the matter radii of ^{9}B [Re(R_m)], but also the charge/matter radii of all states of ^{9}Be, providing direct and convincing evidence of the influence of the valence proton in ^{9}B. Unlike the electrically neutral valence neutron in ^{9}Be, the valence proton in ^{9}B experiences strong Coulomb repulsion from the positively-charged two-alpha-particle core. This force pushes the proton further away from the core, resulting in a charge distribution that extends beyond the matter distribution in the nucleus. This phenomenon is observed for all odd-parity states of the ^{9}B nucleus and contrasts sharply with that of the ^{9}Be nucleus, where the matter radius exceeds the charge radius for most states. This phenomenon has been observed in all odd-parity states of the ^{9}B nucleus and is in stark contrast to that in the ^{9}Be nucleus, where the matter radius exceeds the charge radius in most states.

In Fig. 2, the matter radii of the $K^\pi = 3/2^-_{g.s.}$- and $1/2^-_1$-band states in ^{9}Be and ^{9}B nuclei are shown by the size of circles. We can see that, except for the $J^\pi = 1/2^-$ state in the $K^\pi = 1/2^-_1$ band, those states have similar small-size circles in common, indicating a compact nuclear structure. The exceptionally large radius of the $J^\pi = 1/2^-$ states in the $K^\pi = 1/2^-_1$ band of ^{9}Be and ^{9}B suggests the large expansion of the wave functions due to a low barrier height caused by the small angular momentum, while the ^{9}B state shows a slightly smaller circle compared to ^{9}Be due to the Coulomb barrier. Except for the $J^\pi = 1/2^-$ state in the $K^\pi = 1/2^-_1$ band, all other $K^\pi = 3/2^-_{g.s.}$- and $1/2^-_1$-band states have small radii, which indicate that these band states have compact structures and confirm that they belong to the C type.

Figure 3 shows that the three higher bands labeled $K^\pi = 1/2^-_2$, $K^\pi = 1/2^-_3$, and $K^\pi = 1/2^-_4$ consist of 14 E-type states. The matter radii of these three-band states are commonly larger than those of the low-lying negative-parity-band states belonging to the C type.

Table II provides the same information for even-parity states of the mirror nuclei. Like the odd-parity states, the even-parity states also show that the real parts of the nuclear matter and charge radii are larger than the imaginary parts, with one exception of $J^\pi = 7/2^+_1$ state in the ^{9}B nucleus, in which the imaginary parts are larger than the real parts. The sizes of the matter radii are shown by circles in Fig. 4. The matter radii of the $J^\pi = 3/2^+_1$ states in both ^{9}Be and ^{9}B are very large, even though they are C-type states predicted to have compact nuclear structures. The reason for this is thought to be that the effect of the centrifugal barrier is small due to a small orbital angular momentum, similar to the large matter radii of the $J^\pi = 1/2^-_1$ states in the $K^\pi = 1/2^-_1$ band in Fig. 2. On the other hand, we see large matter radii of $J^\pi = 7/2^+$ and $9/2^+$ states of the $K^\pi = 3/2^+$ band in both ^{9}Be and ^{9}B. This is thought to be because the wave functions are distributed across the barriers of the centrifugal force and the Coulomb force.

B. Channel amplitudes and nuclear cluster structure

From the results of channel amplitudes for Y- and T-type coordinate systems, we can see the components of the ^{5}He $+\alpha$ (^{5}Li $+\alpha$) and ^{8}Be $+n$ (^{8}Be $+p$) configurations in the ^{9}Be (^{9}B) wave functions, respectively. In the calculations, we took the angular-momentum values $l_1 = 0, 1, \cdots, 5$, $L_1 = 0, 1, \cdots, 5$ for the Y-type channel and $l_2 = 0, 2, 4$, $L_2 = 0, 1, \cdots, 5$ for the T-type channel. Below, we denote the channels as $^5\mathrm{He}(l_1, I^\pi_1) + \alpha(L_1)$ and $^8\mathrm{Be}(l_2) + n(l_2, I^\pi_2)$ for ^{9}Be, and as $^5\mathrm{Li}(l_1, I^\pi_1) + \alpha(L_1)$ and $^8\mathrm{Be}(l_2) + p(l_2, I^\pi_2)$ for ^{9}B. We note here that these channel amplitudes of the resonant states are obtained as complex numbers, but, as we see below, the real part is large, while the imaginary part is very small. Furthermore, the amplitudes are insensitive to the complex scaling parameter θ.

First, let us look at the results for the C-type $K^\pi = 3/2^-_{g.s.}$- and $1/2^-_1$-band states shown in Figs. 5 and 6, respectively. The horizontal axis represents the channels by numbering them,

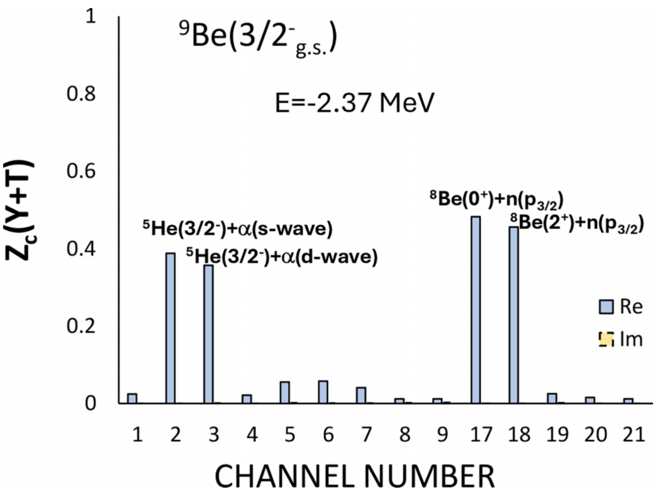

FIG. 5. Channel amplitudes (Z_c) for the ^{9}Be($3/2^-_{g.s.}$) ground state ($E = -2.37$ MeV). The real part (Re) of the amplitude is represented by the light blue bars, and the imaginary part (Im) by the yellow dashed bars.

with the first half representing the Y-type channels and the second half representing the T-type channels, and the vertical axis represents the amplitude of each channel as a bar graph. The real and imaginary parts of the amplitude are represented by the solid and dashed bars, respectively.

Figure 5 shows the results for only the $J^\pi = 3/2^-_{g.s.}$ state of ^{9}Be, because the $K^\pi = 3/2^-_{g.s.}$ band gives results similar to those for other J^π states and states in the ^{9}B nucleus. The channel amplitudes of ^{5}He($3/2^-$) + α(s, d waves) channels in the Y-type system and ^{8}Be(0^+, 2^+) + $n(p_{3/2})$ channels in the T-type system are dominant.

Figure 6 shows the similar distribution for the $J^\pi = 1/2^-$ state of the $K^\pi = 1/2^-_1$ band in the ^{9}Be and ^{9}Be nuclei. Because this $J^\pi = 1/2^-$ state is a resonant one, the calculated amplitudes have finite values in the imaginary part; however, they are very small. The large s-wave amplitude of an alpha cluster in the Y-type system, while slightly reduced in ^{9}B due to the Coulomb force, explains the large matter radii of the $J^\pi = 1/2^-$ states shown in Fig. 2. Other high-spin states of the $K^\pi = 1/2^-_1$ band show distributions similar to those of the $J^\pi = 1/2^-$ states.

Next, we move to the channel amplitudes of the E-type negative-parity bands ($K^\pi = 1/2^-_{2,3,4}$), which commonly exhibit large matter radii. It is noted that the channel amplitudes for both Y- and T-type configurations generally show a similar structural tendency across all odd-parity E-type band states. For clarity and brevity, we select the $J^\pi = 7/2^-_2$ state from the $K^\pi = 1/2^-_4$ band (Fig. 7) and the mirror states. These have dominant amplitudes in the ^{8}Be(2^+) + $N(h_{11/2})$ channel in both ^{9}Be and ^{9}B, where $N = n$ and p in ^{9}Be and ^{9}B, respectively. The amplitudes of the Y-type channels are not concentrated in a specific channel. These results suggest that the E-type states have cluster structures of ^{8}Be $+n$ and ^{8}Be $+p$ in ^{9}Be and ^{9}B, respectively. Since ^{8}Be(2^+) is a resonance state ($\Gamma = 1.5$ MeV [32]) of two α's, the ^{8}Be $+p$ cluster state is considered to be a structure similar to the Hoyle state of

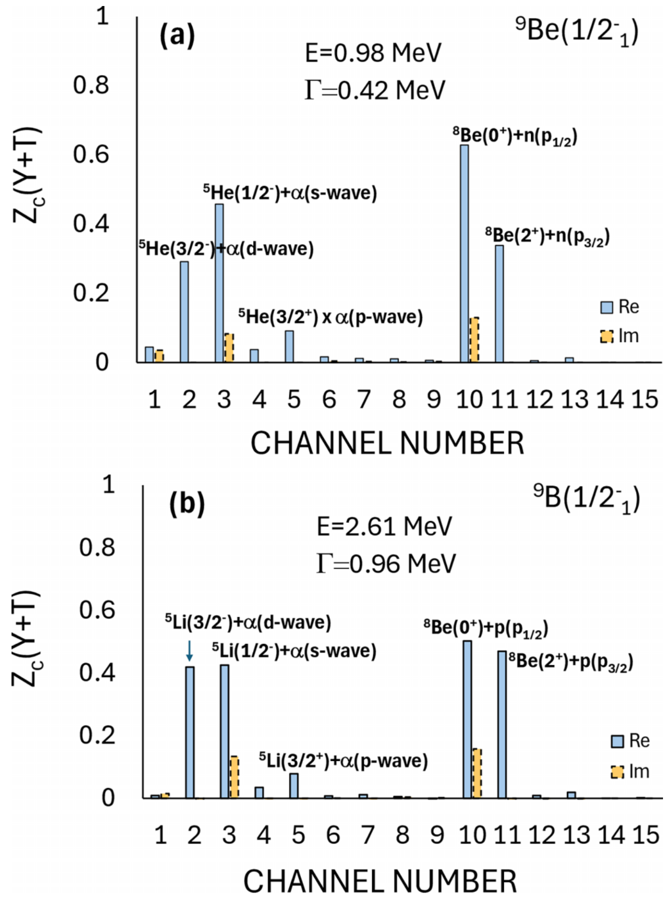

FIG. 6. Channel amplitudes (Z_c) for the low-lying narrow $J^\pi = 1/2^-_1$ mirror resonant states in (a) ^{9}Be ($E = 0.98$ MeV, $\Gamma = 0.42$ MeV) and (b) ^{9}B ($E = 2.61$ MeV, $\Gamma = 0.96$ MeV). The real part (Re) of the amplitude is represented by blue bars, and the imaginary part (Im) by yellow dashed bars.

a 3α system, with two α's and one nucleon loosely bound. Therefore, it is understood that their energies do not show a rigid rotational band structure.

In Figs. 8–10, we show the results of the positive-parity states. Figure 8 displays the channel amplitudes of the $J^\pi = 3/2^+_1$ mirror states that have large matter radii as shown in Fig. 4. In both ^{9}Be and ^{9}B, these states have large amplitudes in the ^{8}Be(2^+) + $N(s_{1/2})$ channel. The s-wave valence nucleon of this channel is coupled with the 2^+ state of ^{8}Be, while the $J^\pi = 1/2^+$ in this band is assigned as a virtual state of ^{8}Be(0^+) + $N(s_{1/2})$. Such an s-wave configuration of the valence nucleon provides a spatially extended structure and the large matter radii.

In Fig. 9, we also show the results for the $J^\pi = 3/2^+_2$ mirror states, which belong to the E type but have slightly smaller matter radii compared to those of the C-type $J^\pi = 3/2^+_1$ states. The $J^\pi = 3/2^+_2$ mirror states have large amplitudes, close to unity, in the ^{8}Be(2^+) + $N(g_{7/2})$ channel in both ^{9}Be and ^{9}B nuclei. The major difference between $J^\pi = 3/2^+_1$ (Fig. 8) and $3/2^+_2$ (Fig . 9) states is the angular momentum of the valence nucleon: $L_2 = 0$ (s wave) in the former and $L_2 = 4$ (g wave) in the latter. Furthermore, the concentration of the

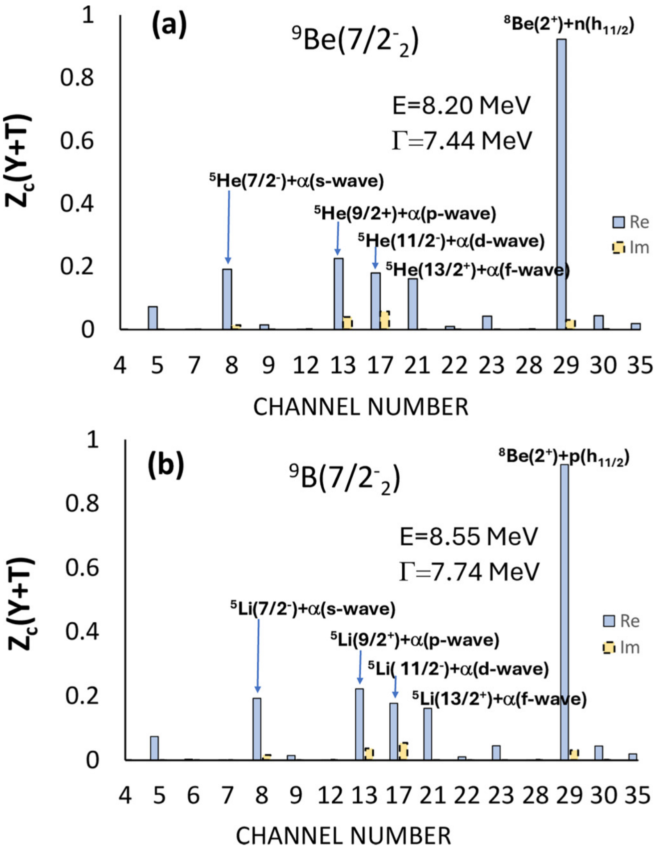

FIG. 7. The results for the high-lying, broad $J^\pi = 7/2_2^-$ state in the $K^\pi = 1/2_4^-$ band for mirror resonant states in (a) ^{9}Be and (b) ^{9}B. The notations are identical to those shown in Fig. 6.

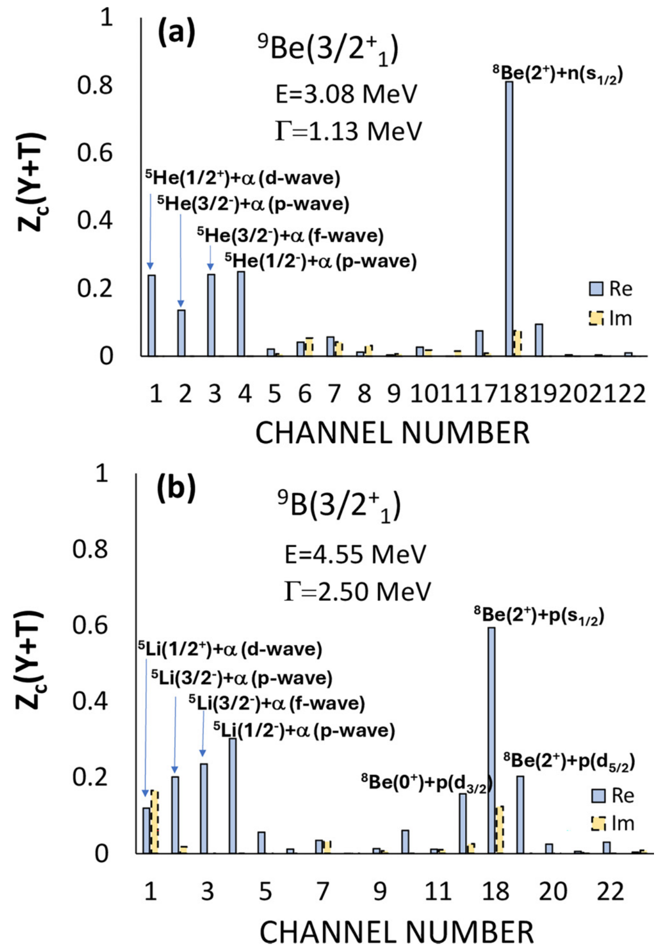

FIG. 8. The results for the low-lying narrow $J^\pi = 3/2_1^+$ mirror resonant states in (a) ^{9}Be and (b) ^{9}B. The notations are the same as those in Fig. 6.

amplitudes in the $J^\pi = 3/2_2^+$ state seems to be larger than that of the $J^\pi = 3/2_1^+$ state, which suggests that the $J^\pi = 3/2_2^+$ state has a more weakly coupled structure of the ^{8}Be $+N$ configuration. Comparing the results in Figs. 8 and 9 also reveals the difference in amplitudes for the Y-type channels. The amplitude of the C-type $J^\pi = 3/2_1^+$ state is distributed in the low-spin channel of ^{5}He (^{5}Li), while the amplitude of the E-type $J^\pi = 3/2_2^+$ state is distributed in the high-spin channel.

In Fig. 10, the channel amplitudes of the $J^\pi = 5/2_1^+$ states are shown, which are primarily characterized by the ^{8}Be$(0^+) + N(d_{5/2})$ configuration. The $J^\pi = 5/2_1^+$ state belongs to the $K^\pi = 1/2_1^+$ band and is classified as the C-type state, similar to the $J^\pi = 3/2_1^+$ state shown in Fig. 8. What the $J^\pi = 5/2_1^+$ state has in common with the $J^\pi = 3/2_1^+$ state is that the amplitudes are concentrated in several channels of both T- and Y-type coordinate systems. More quantitatively, the $J^\pi = 5/2_1^+$ state shows a large concentration in the ^{5}He$(3/2^-) + \alpha$(p-wave) channel in ^{9}Be and in the ^{5}Li$(3/2^-) + \alpha$(p-wave) channel in ^{9}B. The result that the amplitudes of the high angular-momentum channel of the $\alpha + N$ subsystem (^{5}He, ^{5}Li) are larger in the $J^\pi = 5/2_1^+$ state seems to be related to the wave function of this state having a more compact structure and a slightly smaller nuclear radius, as shown in Fig. 3.

IV. DISCUSSION

In previous studies [20,22], we argued that the three-body potential (V_3) plays an important role in describing the ^{9}Be$(1/2^+)$ virtual state. The virtual state provides a large ^{9}Be$(\gamma, n)\,^8$Be photodisintegration cross section, showing excellent agreement with experimental data [18,19], thereby confirming the reliability of our three-body model [20]. However, in the present calculations of low- and high-lying resonant states, structural information such as resonance energies (E^{res}), decay widths (Γ), matter and charge radii (R_m and R_{ch}), and channel amplitudes (Z_c), was largely insensitive to the explicit inclusion of the three-body potential.

As shown in the previous paper [1], the energy levels of the mirror nuclei ^{9}Be and ^{9}B can be classified into C-type and E-type states depending on the Coulomb energy difference. The C-type $K^\pi = 1/2_1^-$-, $3/2_1^-$-, and $1/2_1^+$-band states have been investigated in many previous studies. The understanding there was that one nucleon moves around a ^{8}Be ($\alpha + \alpha$) core, which can be explained by the molecular-orbital picture [2,3,34,35]. The molecular-orbital picture interprets the $J^\pi = 3/2_{\text{g.s.}}^-$ state as a valence neutron occupying a π orbit around the ^{8}Be ($\alpha + \alpha$) core.

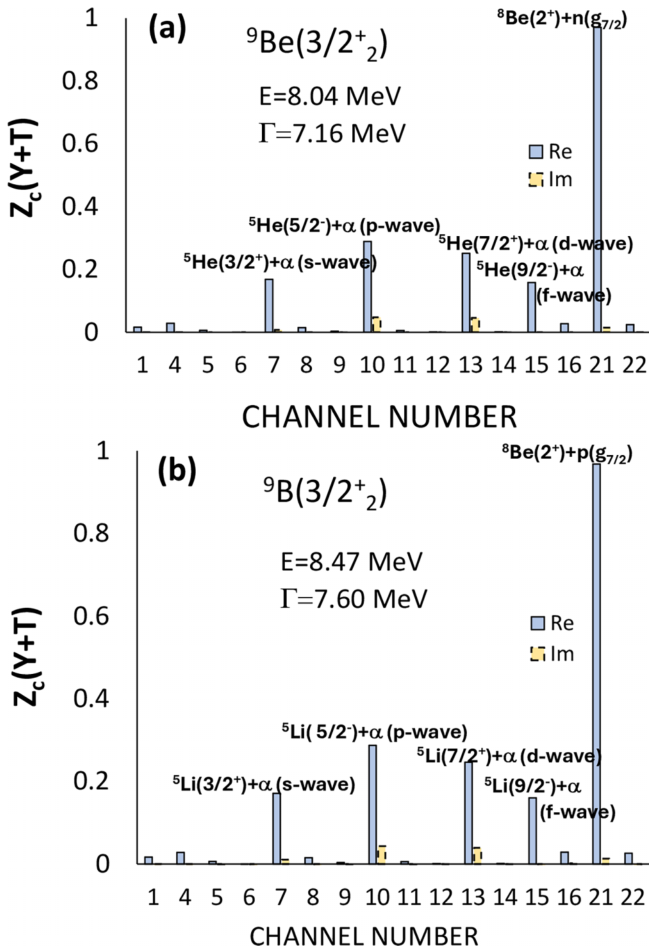

FIG. 9. The results for the high-lying broad $J^\pi = 3/2_2^+$ mirror resonant states in (a) ^{9}Be and (b) ^{9}B. The notations are identical to those shown in Fig. 6.

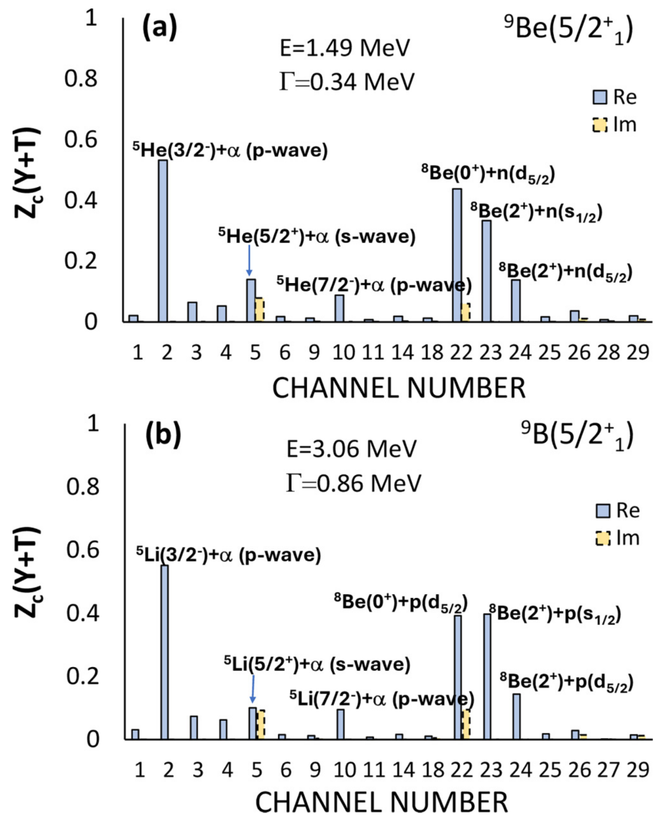

FIG. 10. The results for the low-lying narrow $J^\pi = 5/2_1^+$ mirror resonant states in (a) ^{9}Be and (b) ^{9}B. The notations are the same as those in Fig. 6.

Our results show that the valence neutron occupied the $p_{3/2}$ orbit around ^{8}Be$(0^+, 2^+)$ to the extent of 93.8%, and that the 2^+ excited component of ^{8}Be is comparable to the 0^+ component. This result is consistent with the channel amplitudes of the $(\lambda, \mu) = (3, 1)$ state in the SU(3) model [36,37], which has been shown to have a large overlap with the molecular orbital model wave function [2,3,38]. In the SU(3) model, the (3,1) state gives 53% and 47% for the ^{8}Be$(0^+) \otimes \nu_p$ and ^{8}Be$(2^+) \otimes \nu_p$ components, respectively. The (3,1) state generates two-rotational bands of $K^\pi = 1/2^-$ and $3/2^-$.

Furthermore, the molecular-orbital model links positive-parity states to the σ-orbit. Our channel analysis supports this structural characteristic by quantifying the specific L_2 components of the valence nucleon. The $J^\pi = 3/2_1^+$ (Fig. 8) is dominated by the ^{8}Be$(2^+) \times N(s_{1/2})$ channel, and the $5/2_1^+$ (Fig. 10) has significant $N(d_{5/2})$ and $N(s_{1/2})$ contributions. The presence of these s-wave and d-wave components structurally corresponds to the physical characteristics of the σ-orbit concept.

In our previous calculations, we discovered systematic energy differences between the energy levels corresponding to the mirror symmetry of ^{9}Be and ^{9}B. These systematic Coulomb-energy differences led to the classification of the energy levels into C type and E type. Furthermore, through calculations of the matter and charge radii in this study, we attempted to understand the Coulomb-energy differences in terms of the spatial extent of the wave function, particularly the spatial extent of the valence nucleon. Although the radii of matter and charge differs in each state, and the amplitude of the channels that make up the wave function also differs in each state, we found that no significant differences emerge beyond the energy difference between C-type and T-type. This is thought to be related to the fact that these are resonant states with spatially extended wave functions, which are insensitive to variation of the long-range Coulomb potential. Further analysis of the Thomas-Ehrmann effect [39,40] in resonant states is required for other systems.

V. SUMMARY AND CONCLUSION

We performed the analyses of radii and channel amplitudes of the low- and high-lying resonant states in the mirror nuclei ^{9}Be and ^{9}B, using the CSM within the three-cluster $\alpha + \alpha + N$ model. By including higher values of the angular-momentum quantum numbers (ℓ, L, Λ, J), particularly for odd-parity states, we have successfully identified and characterized two fundamental structural classes: compact C-type states and spatially extended E-type resonance states. This paper is an extension of our previous work [1] and presents the important structural information on the rotational structures and cluster dynamics with different cluster configurations, as well as the persistent nature of the underlying mirror symmetry.

We confirmed the classification of states based on the Coulomb-energy difference (ΔE_C) and calculated the matter and charge radii and the channel amplitudes. The C-type states exhibit large ΔE_C and compact structures, whereas the E-type states are characterized by small ΔE_C and spatially extended configurations. The low-energy odd-parity C-type states are described in both T-type (^{8}Be $+N$) and Y-type [(^{5}He / ^{5}Li $+\alpha$)] cluster-basis sets and exhibit properties consistent with the well-explored molecular-orbital picture. On the other hand, the even-parity C-type states ($J^\pi = 3/2_1^+$, $5/2_1^+$) are considered to have structures dominated by ^{8}Be $+N$ cluster configurations with core excitations [^{8}Be(0^+, 2^+)].

The E-type resonance states have not been discussed in previous experimental and theoretical studies. Those new states have large matter radii, and the calculated resonance widths are also large. The analyses of the channel amplitudes reveal that the amplitudes are concentrated in several channels where the valence nucleon in high angular-momentum orbits around an excited ^{8}Be core, but not in specific channels with Y-type configurations. Furthermore, the $J(J+1)$ plot of the resonance energies does not appear to have a constant moment of inertia like the rigid-body rotation, suggesting a gaslike state of $\alpha + \alpha + N$, similar to a 3α Hoyle state. Further studies on E-type resonance states are needed.

In the ^{9}Be and ^{9}B nuclei, only the ground state of ^{9}Be is a bound state, while all other states are unbound, i.e., resonant states. In the present study, we attempted to investigate the properties of these resonant states using the CSM that is a method similar to that used for bound states. The resonant states with outgoing wave-boundary conditions can be obtained by solving the eigenvalue problem using the CSM, just as in the bound state case. All physical quantities of the obtained resonant states, including energy, matter radius, and channel amplitude, are complex numbers. In this study, we confirmed that the imaginary parts of the matter radii and channel amplitudes of the resonant states are small, and showed that the properties and structure of the resonant states can be discussed using only the real parts. It is interesting and challenging to study the properties and structures of unbound states in other systems by using the present approach.

ACKNOWLEDGMENTS

This work was supported by the National University of Mongolia under Grant Agreement No. P2024-4820, and by JSPS KAKENHI Grants No. JP22K03643, No. JP25H01268, and JST ERATO Grant No. JPMJER2304, Japan. Numerical calculations were achieved through the use of the server at the Nuclear Research Center, National University of Mongolia.

DATA AVAILABILITY

The data that support the findings of this article are not publicly available upon publication because it is not technically feasible and/or the cost of preparing, depositing, and hosting the data would be prohibitive within the terms of this research project. The data are available from the authors upon reasonable request.

[1] M. Odsuren, T. Myo, K. Kikuchi, and K. Katō, Phys. Rev. C **110**, 064316 (2024).
[2] S. Okabe, Y. Abe, and H. Tanaka, Prog. Theo. Phys. **57**, 866 (1977).
[3] S. Okabe and Y. Abe, Prog. Theo. Phys. **61**, 1049 (1979).
[4] K. Arai, P. Descouvemont, D. Baye, W. N. Catford, Phys. Rev. C **68**, 014310 (2003).
[5] P. Descouvemont, Eur. Phys. J. A **12**, 413 (2001).
[6] R. Alvarez-Rodriguez, A. S. Jensen, E. Garrido, and D. V. Fedorov, Phys. Rev. C **82**, 034001 (2010).
[7] A. V. Nesterov, V. S. Vasilevsky, and T. P. Kovalenko, Phys. At. Nucl. **77**, 555 (2014).
[8] J. Casal, M. Rodriguez-Gallardo, J. M. Arias, and I. J. Thompson, Phys. Rev. C **90**, 044304 (2014).
[9] Y. H. Yang, Y. G. Ma, S. M. Wang, B. Zhou, and D. Q. Fang, Phys. Rev. C **108**, 044307 (2023).
[10] W. John and J. M. Prosser, Phys. Rev. **127**, 231 (1962).
[11] M. Fujishiro, T. Tabata, K. Okamoto, and T. Tsujimoto, Can. J. Phys. **60**, 1672 (1982).
[12] H. Utsunomiya, Y. Yonezawa, H. Akimune, T. Yamagata, M. Ohta, M. Fujishiro, H. Toyokawa, and H. Ohgaki, Phys. Rev. C **63**, 018801 (2000).
[13] H. Akimune, M. Fujimura, M. Fujiwara, K. Hara, T. Ishikawa, T. Kawabata, H. Utsunomiya, T. Yamagata, K. Yamasaki, and M. Yosoi, Phys. Rev. C **64**, 041305(R) (2001).
[14] O. Burda, P. von Neumann-Cosel, A. Richter, C. Forssen, and B. A. Brown, Phys. Rev. C **82**, 015808 (2010).
[15] J. H. Gibbons, R. L. Macklin, J. B. Marion, and H. W. Schmitt, Phys. Rev. **114**, 1319 (1959).
[16] V. Efros and J. Bang, Eur. Phys. J. A **4**, 33 (1999).
[17] E. Garrido, D. V. Fedorov, and A. S. Jensen, Phys. Lett. B **684**, 132 (2010).
[18] C. W. Arnold, T. B. Clegg, C. Iliadis, H. J. Karwowski, G. C. Rich, J. R. Tompkins, and C. R. Howell, Phys. Rev. C **85**, 044605 (2012).
[19] H. Utsunomiya, S. Katayama, I. Gheorghe, S. Imai, H. Yamaguchi, D. Kahl, Y. Sakaguchi, T. Shima, K. Takahisa, and S. Miyamoto, Phys. Rev. C **92**, 064323 (2015).
[20] M. Odsuren, Y. Kikuchi, T. Myo, M. Aikawa, and K. Katō, Phys. Rev. C **92**, 014322 (2015).
[21] M. Odsuren, T. Myo, and K. Katō, Phys. Rev. C **107**, 044003 (2023).
[22] Y. Kikuchi, M. Odsuren, T. Myo, and K. Katō, Phys. Rev. C **93**, 054605 (2016).
[23] K. Ho, Phys. Rep. **99**, 1 (1983).
[24] J. Aguilar and J. M. Combes, Commun. Math. Phys. **22**, 269 (1971); E. Balslev and J. M. Combes, *ibid.* **22**, 280 (1971).
[25] S. Aoyama, T. Myo, K. Katō, and K. Ikeda, Prog. Theor. Phys. **116**, 1 (2006).

[26] T. Myo, Y. Kikuchi, H. Masui, and K. Katō, Prog. Part. Nucl. Phys. **79**, 1 (2014).

[27] T. Myo and K. Katō, Phys. Rev. C **107**, 014301 (2023).

[28] T. Myo and K. Katō, Prog. Theor. Exp. Phys. **2020**, 12A101 (2020).

[29] S. Saito, Prog. Theor. Phys. **40**, 893 (1968); **41**, 705 (1969); Suppl. **62**, i (1977).

[30] E. Hiyama, Y. Kino, and M. Kamimura, Prog. Part. Nucl. Phys. **51**, 223 (2003).

[31] W. Nörtershäuser, D. Tiedemann, M. Žáková, Z. Andjelkovic, K. Blaum, M. L. Bissell, R. Cazan, G. W. F. Drake, C. Geppert, M. Kowalska, *et al.*, Phys. Rev. Lett. **102**, 062503 (2009).

[32] D. Tilley, J. Kelley, J. Godwin, D. Millener, J. Purcell, C. Sheu, and H. Weller, Nucl. Phys. A **745**, 155 (2004).

[33] I. Tanihata, T. Kobayashi, O. Yamakawa, S. Shimoura, K. Ekuni, K. Sugimoto, N. Takahashi, T. Shimoda, and H. Sato, Phys. Lett. B **206**, 592 (1988).

[34] W. von Oertzen, Z. Phys. A **357**, 355 (1997).

[35] W. von Oertzen, Martin Freer, and Yoshiko Kanada-En'yo, Phys. Rep. **432**, 43 (2006).

[36] J. P. Elliott, Proc. Roy. Soc, A **245**, 562 (1958).

[37] M. Harvey, Adv. Nucl. Phys. **1**, 67 (1968).

[38] H. Furutani, *et al.*, Prog. Theor. Phys. Suppl. **68**, 193 (1980).

[39] R. G. Thomas, Phys. Rev. **88**, 1109 (1952).

[40] J. B. Ehrman, Phys. Rev. **81**, 412 (1951).